Talanta 298 (2026) 128982

Contents lists available at ScienceDirect

Talanta

journal homepage: www.elsevier.com/locate/talanta

Deep learning enhanced label-free cervical screening via stimulated Raman cytology

Yingjie He [a,1], Mingming Zhao [b,1,2], Hao Zhang [c], Minbiao Ji [a,*], Chao Wang [b,**]

[a] State Key Laboratory of Surface Physics and Department of Physics, Key Laboratory of Micro and Nano Photonic Structures (Ministry of Education), Endoscopy Center and Endoscopy Research Institute, Zhongshan Hospital, Fudan University, Shanghai, 200433, China
[b] Department of Gynecology, Obstetrics and Gynecology Hospital, Fudan University, China
[c] Department of Pathology, Obstetrics and Gynecology Hospital, Fudan University, China

ARTICLE INFO

Keywords:
Cervical cancer
Cervical cytology screening
Label-free cytology
Stimulated Raman scattering
Deep-learning

ABSTRACT

Cervical cancer screening remains pivotal for early detection and effective disease management, yet conventional cytopathological methods relying on stained cell-smear analysis face critical limitations in diagnostic throughput and sensitivity. We present a stain-free Visual-Aided Diagnosis via Stimulated Raman Cytology (VAD-SRC) platform that enables rapid cervical cell screening through simultaneous chemical and morphological profiling. By capturing intrinsic biomolecular contrast via stimulated Raman scattering (SRS) microscopy, our platform establishes malignancy-associated cellular fingerprints through quantitative analysis. Integrated with a deep convolutional neural network architecture, VAD-SRC achieves superb diagnostic performance (98.5 % accuracy, 100 % sensitivity) on an independent test set for binary classification of benign versus malignant cases. Moreover, its high-resolution segmentation function automates the identification of individual cancer cells within a mixture of five cell types: normal cells, leucocytes, low-grade squamous intraepithelial lesion (LSIL), high-grade squamous intraepithelial lesion (HSIL), and squamous cervical cancer (SCC) cells. This advancement offers promising potential for cervical cancer screening and visual assessments within cytopathology workflows, enhancing diagnostic efficiency and precision.

1. Introduction

Cervical cancer (CC) remains a critical global health challenge as one of the three most common malignant tumors of female reproductive system, causing more than 300,000 annual deaths worldwide [1], maintaining its status as the second leading cause of cancer-related mortality in women aged 20–39 [2]. Despite the success of Pap smear screening and human papillomavirus (HPV) vaccination programs, the disease continues to pose a significant burden, particularly in regions with limited access to early screening [3–6]. While the ThinPrep Cytologic Test (TCT) has been widely adopted, its diagnostic value is limited by inter-observer variability, modest sensitivity for high-grade lesions, and lengthy processing times [7–10]. According to the America Cancer Society (ACS) management guidelines [11], low grade squamous intraepithelial lesion (LSIL) is considered benign and typically monitored without immediate intervention, whereas high grade squamous intraepithelial lesion (HSIL) and squamous cervical cancer (SCC) are categorized as malignant, necessitating definitive diagnosis and treatment. The morphological similarities between LSIL and reactive changes frequently results in diagnostic ambiguity, highlighting critical gaps in current diagnostic frameworks and the urgent need for more accurate and efficient cervical cytologic screening modalities.

Various label-free optical methods have been widely investigated for cervical cell imaging and cancer screening. While techniques like optical coherence tomography (OCT), autofluorescence microscopy, and second harmonic generation (SHG) microscopy provide structural insights, they lack chemical specificities of cells [12,13]. Spontaneous Raman scattering spectroscopy, despite its biochemical sensitivity, suffers from weak scattering cross-section and slow acquisition speed for efficient histologic diagnosis [14–16]. Coherent anti-Stokes Raman scattering

* Corresponding author.
** Corresponding author. Chao Wang.
E-mail addresses: minbiaoj@fudan.edu.cn (M. Ji), wangchao1585@fckyy.org.cn (C. Wang).
[1] Y.H. and M.Z. contributed equally to this work.
[2] Current address: Department of Gynecology, Shanghai First Maternity and Infant Hospital, School of Medicine, Tongji University, Shanghai, China.

https://doi.org/10.1016/j.talanta.2025.128982
Received 19 May 2025; Received in revised form 6 October 2025; Accepted 12 October 2025
Available online 13 October 2025

(CARS) microscopy struggles with non-resonant background interference, complicating accurate quantification of chemical concentrations [17]. Despite these challenges, the chemical information associated with cellular metabolic reprogramming is critically important for tumor progression [18], including the energy demand of tumor proliferation and invasion that could alter the energy supply pathways through anaerobic glycolysis and lipid metabolism, etc. [19]. Hence intracellular chemical compositions (such as lipid and protein) may be used to differentiate normal cells from tumor cells. However, the analysis of conventional cervical cytology is either limited by external labeling [20–22] or constrained by imaging speed and resolution [23–26].

As a novel imaging technique, stimulated Raman scattering (SRS) microscopy amplifies Raman signal by orders of magnitude through coherent stimulated emission process, achieving high sensitivity and imaging speed, while retaining chemical resolution based on the spectral fingerprints of intrinsic molecules [27–30]. Thus, SRS microscopy offers advantages in rapid label-free chemical imaging at the single-cell level with diffraction-limited spatial resolution. Recent researches have demonstrated that SRS integrated with artificial intelligence (AI) algorithms holds promise in clinical screening and rapid diagnosis of tumor on unprocessed tissues, with potential applications in intraoperative histopathology for various types of human cancers [31–36]. Although single-cell SRS imaging has also been shown in the diagnosis of peritoneal metastasis of gastric cancer [37], it heavily relied on the numerical analysis of multiple cytological features using K-means and SVM (Support Vector Machine) algorithms. From the perspective of pathologists, there exist distinct differences between cytological and histological examinations in clinical practice [38–40]. While direct image-guided cytologic examination is more favored in clinical settings due to its specificity [41], it also provides valuable diagnostic confirmation opportunities based on AI-recognized abnormal cells, alongside predictive results [42–44].

In this study, we developed a Visual-Aided Diagnosis via Stimulated Raman Cytology (VAD-SRC) platform for cervical cancer screening. Unlabeled cellular images containing lipid and protein distributions were captured, and chemical analysis was performed on various cell types to investigate the correlation between cytological features and diagnostic performance of the neural network. A convolutional neural network (CNN)-based classification model successfully categorized images into benign and malignant groups, achieving an accuracy of 98.5 % and a sensitivity of 100 %. Additionally, a segmentation network was implemented to visualize individual cancer cells within the malignant group, aiding pathologists in final decision-making for rapid diagnosis in cervical cytology screening.

2. Materials and methods

2.1. Collection and preparation of cervical cells

The study was approved by the Institutional Ethics Committee of the Obstetrics and Gynecology Hospital of Fudan University, School of Medicine with written informed consent (approval no. 2024–227). Cell samples were collected from 41 individuals undergoing cervical cancer screening at Obstetrics and Gynecology Hospital of Fudan University, including 8 healthy controls and 33 patients pathologically confirmed with cervical malignant lesions. For each individual, cervical cell samples were collected using a cervical cytobrush. Half of the samples were used for cytological examination, and further testing was determined based on the results, ultimately leading to the clinical diagnosis of the patient. The other half of the samples were immediately prepared into smears without additional fixation or storage, and subjected directly to SRS imaging. Specifically, the samples were rinsed with phosphate-buffered saline, and centrifuged at 2000 rpm for 3 min. A cell suspension (approximately 10 μL) was then dropped onto a glass slide and evenly spread for SRS microscopy examination, followed by analysis using VAD-SRC. The number of cells in each group was maintained in a balanced distribution across different analytical tasks (e.g., Student's t-test, classification model, and segmentation model).

2.2. SRS imaging

We used the following setup for SRS imaging: a femtosecond optical parametric oscillator (Insight DS+, Newport) laser was employed as the light source, with a fixed-wavelength beam (1040 nm, ~200 fs) serving as the Stokes beam and a tunable beam (680–1300 nm, ~150 fs) functioning as the pump beam. The Stokes beam and pump beam were linearly chirped to picoseconds using SF57 glass rods, providing sufficient spectral resolution. The Stokes beam was modulated by an electro-optic modulator at a frequency of 20 MHz. The two spatially and temporally overlapped beams were focused onto the sample through a laser scanning microscope (FV1200, Olympus) and a water immersion objective lens (UPLSAPO 60XWIR, NA 1.2 water, Olympus) to induce the SRS process. The stimulated Raman loss signal was detected by a homemade back-biased photodiode and the electronic signal was further demodulated with a lock-in amplifier (HF2LI, Zurich Instruments) to form images. The motorized delay stage selected the target Raman frequency by adjusting the pulse time delay between the two beams. For cellular imaging, we utilized the Raman shifts at 2845 cm^{-1} and 2930 cm^{-1}. Based on the spectral differences of lipids and proteins at these two wavenumbers, we obtained SRS images of lipid and protein distributions through a linear decomposition algorithm, generating a two-color SRS image with lipids represented in green and proteins in blue. All images were acquired at 512 × 512 pixels, with a pixel dwell time of 2 μs. The system's spatial resolution was 350 nm. The laser power incident on the sample was as follows: pump 30 mW and Stokes 30 mW.

2.3. Visual-aided diagnostic model

To achieve visual-aided diagnosis of cervical cells, we designed a deep learning algorithm that includes two models: a classification model and a segmentation model. The model was developed using the PyTorch framework compiled in Python. The core of the classification model is the "ResNet50" network, which consists of 49 convolutional layers and one fully connected layer. The basic building block of the network is the residual block, with each residual block consisting of three convolutional layers. The collected SRS images are used as input, and the model outputs the predicted results along with their probabilities. The core of the segmentation model is the "DeepLabV3+" network, which employs an encoder-decoder structure. The encoder part is responsible for feature extraction. Its main body consists of a deep convolutional neural network (DCNN) with atrous convolutions, along with the atrous spatial pyramid pooling module (ASPP). The decoder part progressively restores spatial information through upsampling. SRS images are used as input, and the output of the network is a segmentation map, where each pixel in the input image is assigned a class label. The five types of cells are assigned five class labels with color coding. All deep learning tasks were conducted on a workstation equipped with an NVIDIA GTX 1080Ti GPU (11 GB memory). Model development and training were implemented in Python 3.11.5 using PyTorch 2.0.1.

In the dataset preparation process, for the classification model, pathologists pre-annotated the SRS images into benign/malignant categories; for the segmentation model, pathologists pre-annotated the regions of different cells within the images to generate segmentation masks. The datasets are subsequently divided into training and testing sets. The test set images were independent of the training process at the patient level. The remaining images were used for model development. Within this subset, fivefold cross-validation was applied to separate training and validation subsets for parameter optimization. To reduce overfitting and balance class distribution, data augmentations (rotation, flipping, and adjustment of contrast and brightness) were applied prior to training. Accuracy, the receiver operating characteristic (ROC), area under the curve (AUC), and confusion matrix were used to evaluate the

performance of classification models. Intersection over union (IoU), recall, precision and dice coefficient were used to evaluate the performance of segmentation model. The network was initialized as follows: the learning rate for the classification model was set to 0.075, while the learning rate for the segmentation model was set to 0.007. Stochastic Gradient Descent (SGD) was chosen as the optimizer, and CrossEntropyLoss was used as the loss function.

2.4. Images processing and analysis

For SRS images, the intensity distributions of lipids and proteins in cells were obtained using a linear decomposition algorithm. ImageJ was then utilized to extract the area, total lipid intensity, total protein intensity, average lipid intensity, average protein intensity, and the protein/lipid ratio for normal cells, leucocytes, LSIL, HSIL, and SCC cells. The PCA algorithm was used to reduce the dimension of cytological feature data, and K-means algorithm was used to cluster the data after dimensionality reduction. Both PCA and K-means were performed by Origin. A Student's t-test was conducted to compare cytological feature data between groups, yielding p values (adjusted by Holm–Sidak), confidence intervals (CI) and R values. Spearman correlation analysis was performed to analyze the cytological features of cells at different degrees of malignancy, obtaining r values and p values. All analyses were executed using SPSS.

Prior to deep learning analysis, all raw SRS images were normalized and standardized (mean-centered and variance-scaled) to stabilize model training. Data augmentation methods were also applied to expand dataset diversity and reduce overfitting.

3. Results and discussion

3.1. Workflow of VAD-SRC

The main goal of our study is to develop a rapid, accurate and image-guided cervical cancer screening method. SRS microscopy was employed to capture intrinsic molecular information without staining. A deep learning-based visual-aided diagnostic system was developed to reduce pathologists' workload and provide more objective diagnoses. Fig. 1 illustrates the workflow of VAD-SRC. First, cervical cell specimens were collected from patients using sample brushes, which were then smeared onto glass slides for direct SRS imaging (Fig. 1a) based on the Raman bands of the CH_2 (2845 cm^{-1}) and the CH_3 (2930 cm^{-1}) vibrations. Such frequency selection has been widely adopted to extract protein and lipid distributions in biological speciemens based on their characteristic SRS spectra (Supplementary Fig. S1) [45–47]. The dual-channel images were decomposed into lipid (green) and protein (blue) distributions to obtain two-color SRS images using a linear combination algorithm (Fig. 1b) [48,49]. Then the images were fed into a convolutional neural network (CNN)-based diagnostic system to conduct both the classification and segmentation tasks (Fig. 1c). In this study, cervical cells were classified into binary groups (benign/malignant) according to clinical criteria: those containing only normal cells, leucocytes, and LSIL cells were classified as benign; whereas those showing any SCC or HSIL cells were classified as malignant [50]. The malignant group was further processed by the segmentation model to delineate individual HSIL and SCC cells within the whole-slide image. By doing so, the AI-assisted visualization of malignant cells allows pathologists to rapidly identify target cells to make final diagnostic decision, helping to avoid examination on a large number of cells with improved diagnostic accuracy.

3.2. SRS imaging and Pap smear of cells

Cervical cell specimens were imaged with SRS microscopy to map out the chemical and morphological profiles in a label-free manner. To directly compare SRS with Pap smears in revealing cytologic features of various cervical cells, we imaged each sample with the two modalities: SRS microscopy without labeling, and Pap staining followed by bright-field optical microscopy. Fig. 2 shows the comparison between SRS and Pap smear results of five cell types, including normal cells (Fig. 2a), leucocytes (Fig. 2b), LSIL (Fig. 2c), HSIL (Fig. 2d) and SCC (Fig. 2e) cells. It can be seen that SRS images readily show the distinct cell morphology and chemical contrast of each cell types. Moreover, they demonstrate high consistency with Pap smears in cytologic diagnosis as recognized by pathologists. Normal cervical cells tend to have the largest size and higher protein content (blue), lymphocytes appear the smallest in size. LSIL cells clearly exhibit perinuclear cytoplasmic clearing (koilocytosis, arrow) and demonstrate an increased nucleus-to-cytoplasm (N/C) ratio relative to normal cells. In contrast, both HSIL and SCC cells show an even larger N/C ratio compared to LSIL cells. HSIL cells are

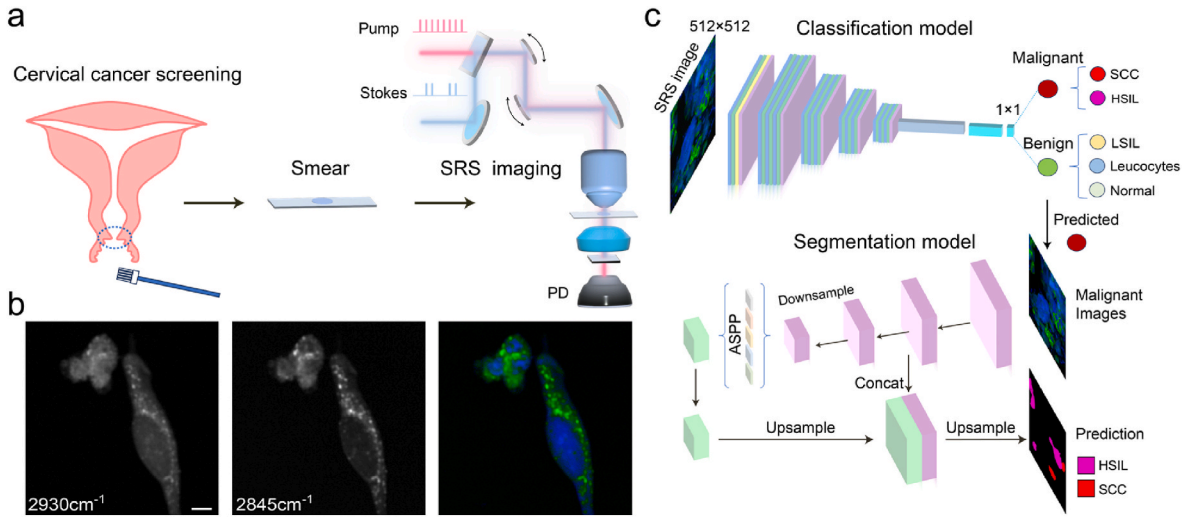

Fig. 1. Workflow of visual-aided diagnostic system based on stimulated Raman cytology (VAD-SRC). a, Taking cell smears from patients undergoing cervical cancer screening for SRS imaging. **b,** Cells were imaged at 2930 cm^{-1} (left) and 2845 cm^{-1} (middle). A linear decomposition algorithm of the two raw images was used to compute the distribution of lipid (green) and protein (blue), merging into a two-color SRS image (right). Scale bars: 5 μ m. **c,** Visual-aided diagnostic system consists of two components: a classification model and a segmentation model. The classification model genereates binary prediction of benign versus malignant, and the segmentation model subsequently identifies individual cancer cells within the malignant group. (For interpretation of the references to color in this figure legend, the reader is referred to the Web version of this article.)

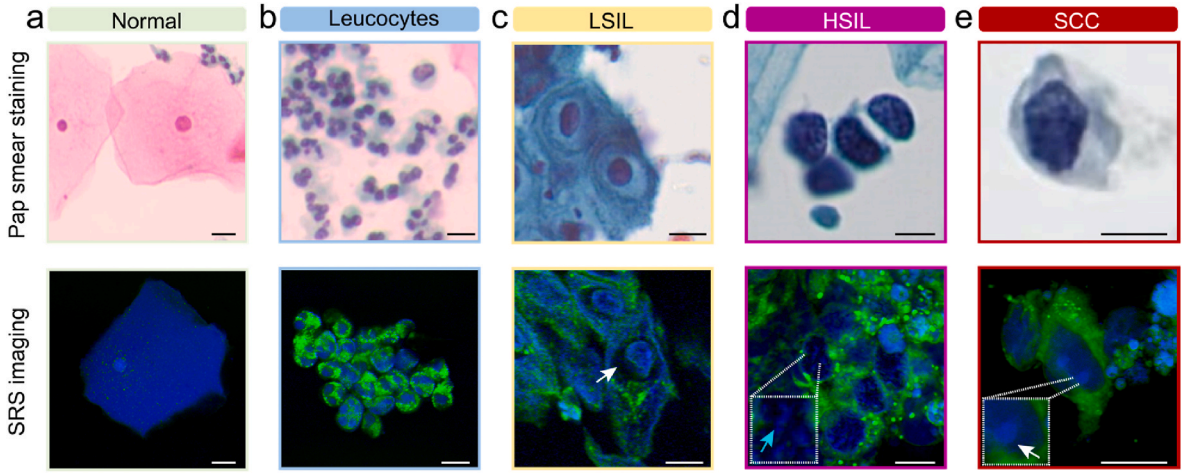

Fig. 2. Pap smear staining and SRS imaging of different types of cervical cells. a-e, Normal cells, leucocytes, low grade squamous intraepithelial lesion (LSIL) cells (koilocytosis, arrow), high grade squamous intraepithelial lesion (HSIL) cells (coarse chromatin displaying granular pattern, arrow), squamous cervical cancer (SCC) cells (nucleoli, arrow). The region of interest is shown with a magnified view inside the dashed box. Scale bars: 10 μ m.

characterized by coarse chromatin displaying a uniformly distributed granular pattern (arrow), whereas SCC cells frequently present with prominent nucleoli (arrow) [50,51]. Additionally, LSIL, HSIL, and SCC cells show an elevated lipid content compared to normal cells (green). The combined spatio-chemical information is essential for subsequent feature analysis and deep-learning models in cervical cytopathology and cell typing.

3.3. Quantitative morphological and chemical characterization of cervical cells

We next performed detailed cytologic and biochemical characterizations of normal cells, leucocytes, LSIL, HSIL and SCC cells. Taking advantage of SRS microscopy in quantitative chemical analysis of unprocessed cervical cells, we were able to extract six key quantities for cell typing, including the area, total protein intensity, total lipid intensity, mean protein intensity, mean lipid intensity, and protein/lipid ratio. Direct comparisons between the five cell types were made using Student's t-test (adjusted p-values; $p < 0.05$ considered significant). As shown in Fig. 3a, normal cells appear the largest with highest total protein and lipid intensity, leucocytes are the smallest in size with lowest total protein and lipid intensity. Significant differences in area, total protein, total lipid and protein/lipid ratio between all the groups ($p < 0.05$) were observed. The average protein intensity of normal cells is higher than leucocytes ($p < 0.05$, 95 % CI: 41.08 to 319.0), and that of HSIL is higher than LSIL($p < 0.001$, 95 % CI: 155.2 to 389.7)/SCC cells ($p < 0.001$,95 % CI: 2.111 to 298.1). No significant difference in average protein intensity exists between normal cells and LSIL/HSIL/SCC cells, nor between LSIL cells and leucocytes/SCC cells. The average lipid intensity shows significant differences among all the groups ($p < 0.05$) except that between leucocytes and HSIL cells. In Student's t-test, R-value could be extracted to reflect the correlation of differences between data, with larger values indicating greater disparity. We plotted heat maps using the R-values to show the magnitude of differences between groups with statistically significant disparities, thereby facilitating further analysis of these differences. As shown in Fig. 3b, the differences in cell area, total protein, and total lipid intensity between normal cells and other cell types were the most pronounced. In terms of average lipid intensity, although both HSIL ($p < 0.001$, 95 % CI: 312.4 to 432.1) and SCC ($p < 0.001$, 95 % CI: 145.3 to 230.0) cells show significant distinction from LSIL cells (Fig. 3a), it is evident that the HSIL/LSIL difference is greater than that of HSIL/SCC cells (Fig. 3b). For average protein intensity, HSIL/LSIL difference is greater than that of SCC/LSIL cells. However, for total protein intensity, HSIL/LSIL difference is weaker than that of SCC/LSIL cells. The difference in protein/lipid ratio between HSIL and SCC cells is less obvious than that between the other cell types.

To investigate the connection between cellular characteristics (cell morphology and chemical composition) and the degree of malignancy of cervical cells, we performed Spearman's correlation analysis for normal, LSIL, HSIL, and SCC cells. Results in Fig. 3c indicate that cell area ($r = -0.8827$, $p < 0.0001$), total protein intensity ($r = -0.9071$, $p < 0.0001$), total lipid intensity ($r = -0.7611$, $p < 0.0001$), and protein/lipid ratio ($r = -0.7323$, $p < 0.0001$) were negatively correlated with the degree of malignancy; while the average lipid intensity was positively correlated with the degree of malignancy ($r = 0.6766$, $p < 0.0001$), and the average protein intensity showed no significant correlation with malignancy ($p > 0.05$). The above statistical results indicate that cell morphology and biochemical compositions differ significantly between various cervical cell types, and are closely related to the degree of malignancy.

3.4. Automated diagnoses with classification model

We further employed AI-assisted cervical cancer cytological screening leveraging both morphological and chemical cellular characteristics of various cell types. We first tested dimensionality reduction on the original feature dataset using principal component analysis (PCA) algorithm to produce primary components PC1 and PC2 (>90 % of total features), followed by K-means clustering algorithm to divide the data into two distinct populations (Fig. 4a). However, such unsupervised paradigm segregated normal cells from all pathological subtypes (Fig. 4b), failing to achieve the clinically critical benign/malignancy discrimination.

We therefore implemented a supervised deep learning framework using a residual neural network (ResNet50) optimized for diagnostic classification based on SRS images containing integrated cytomorphological and biochemical signatures. A curated dataset of 700 SRS images from 41 patients was annotated by pathologists based on standardized benign/malignancy criteria (Fig. 4c): images containing any HSIL or SCC cells were classified as malignant, while those containing only normal cells, leucocytes, and LSIL cells labeled as benign cases.

To mitigate class imbalance inherent in cytological samples [52], we strategically oversampled malignant cases during model development, achieving an 80.5 %:19.5 % malignant-to-benign ratio in the training cohort (Supplementary Fig. S2a). In terms of number of images, the malignant/benign distribution is 44.3 %:55.7 % (Supplementary Fig. S2b). The dataset was partitioned into training (90 %) and holdout test (10 %) sets, with rigorous separation maintained throughout

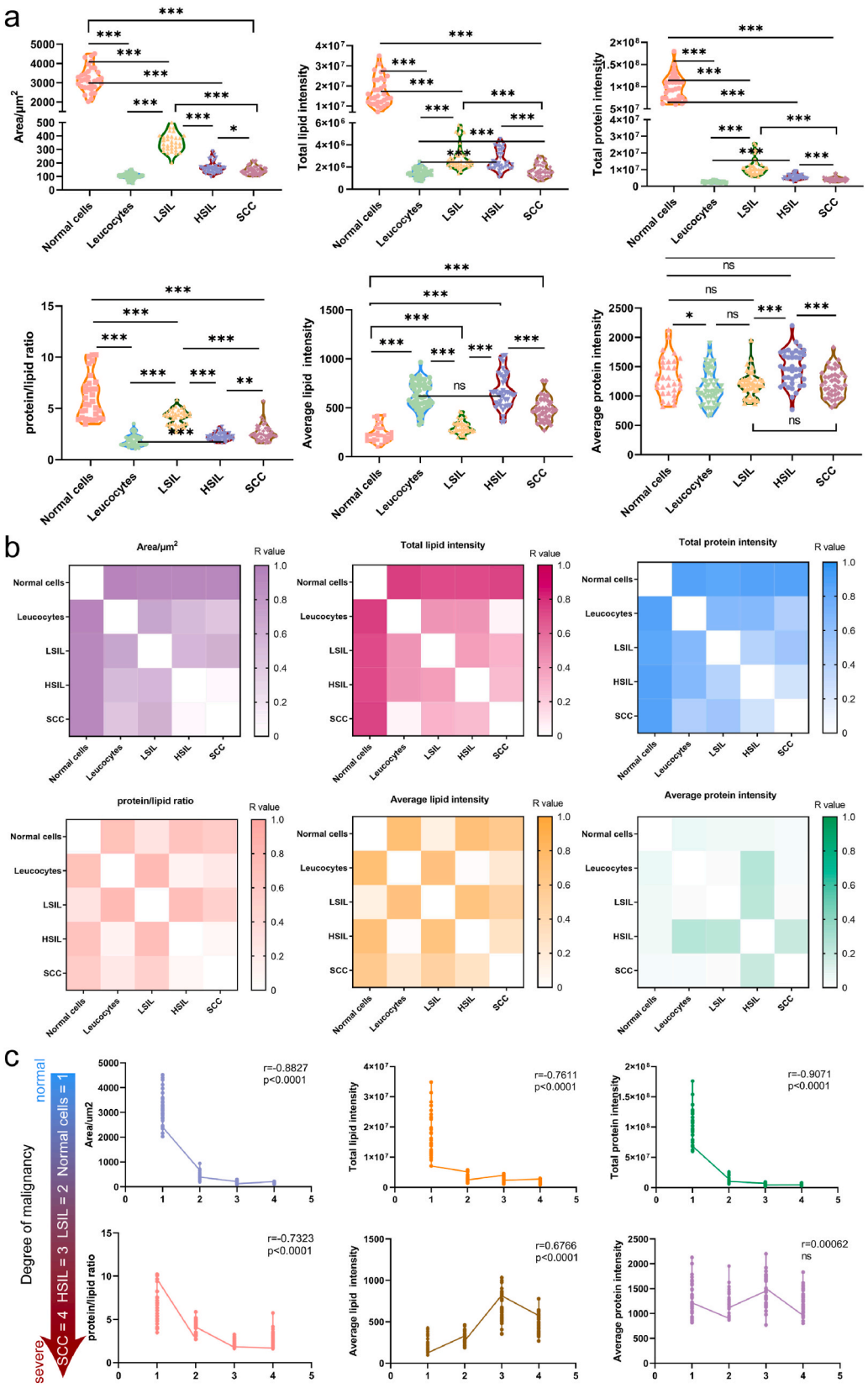

Fig. 3. Quantitative characterization of cell morphology and chemical composition. a, Differential analysis of cell area, total lipid intensity, total protein intensity, protein/lipid ratio, average lipid intensity and average protein intensity in each group using *t*-test. ***p < 0.001, **p < 0.01, *p < 0.05, ns: no significant difference (p-values were adjusted using the Holm–Sidak method). **b,** Heatmap of area, total lipid intensity, total protein intensity, protein/lipid ratio, average lipid intensity and average protein intensity in each group based on R values. **c,** Spearman correlation analysis between cellular characteristics and the degree of malignancy of normal cells (1), LSIL (2), HSIL (3), and SCC (4) cells.

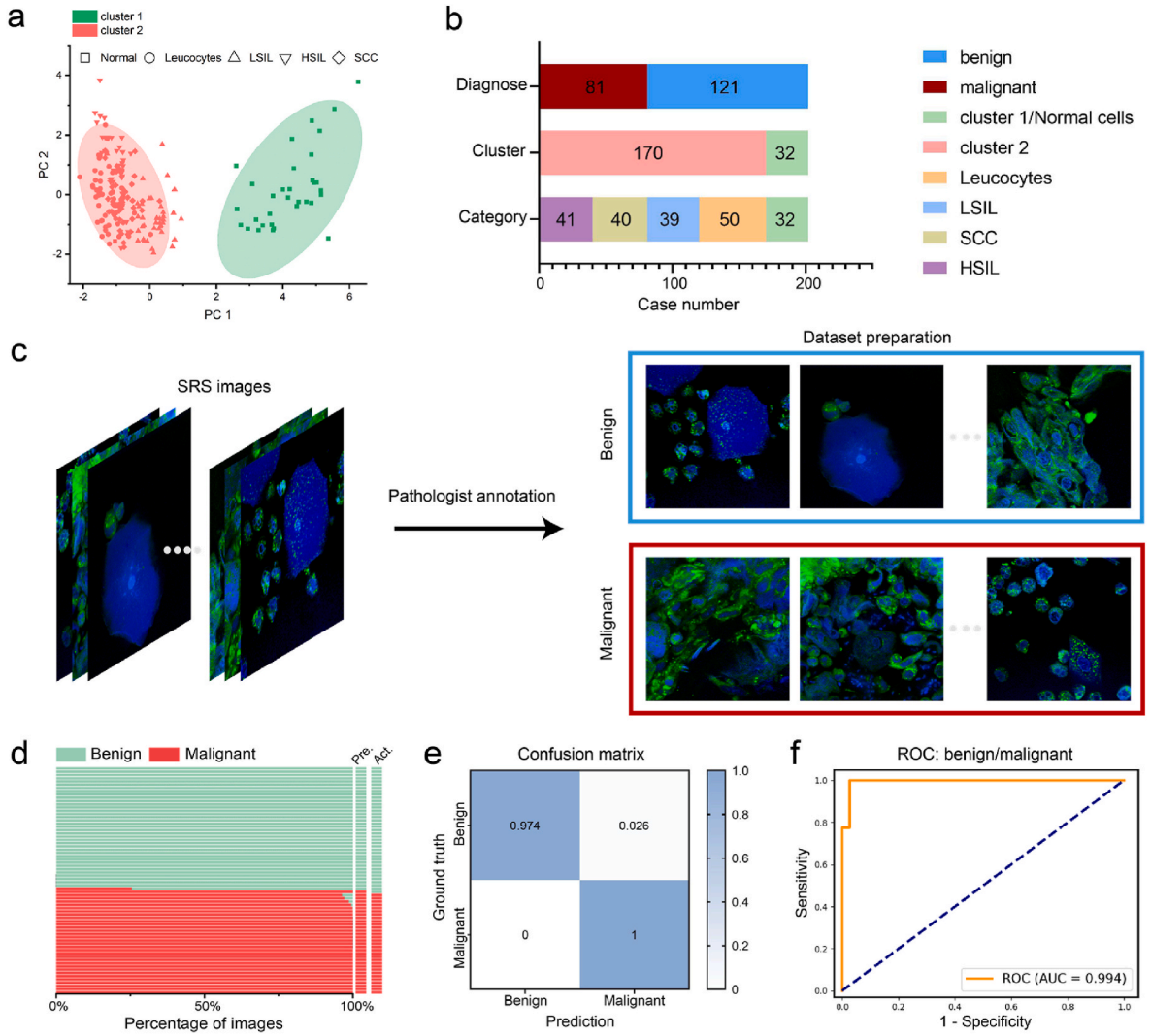

Fig. 4. Comparison between unsupervised model and supervised model for classification diagnosis. a, Cellular characteristics data was reduced in dimensionality using PCA, followed by clustering through the unsupervised K-means algorithm. **b,** Comparison of the diagnostic results based on customized clinical standards for various cell types with clustering results. **c,** Pathologists pre-annotated SRS images for datasets preparation. The images were classified into benign and malignant categories. **d,** Diagnostic results of test set images using supervised network (ResNet50), compared with true pathology results. **e,** Confusion matrix of diagnosis between the classification model and pathologists. **f,** ROC analysis of the results from classification model. AUC: area under the curve.

validation. For data partitioning, we designated data from 5 patients (a total of 70 images) as an independent test set, which was strictly excluded from all training and validation procedures to ensure unbiased evaluation on unseen patients. The remaining images were used for model development, where five-fold cross-validation was applied between the training (80 %) and validation (20 %) subsets to optimize model parameters and maximize data utilization. Training images underwent augmentation (rotation, flipping, contrast/brightness adjustment) to generate 6930 samples.

The ResNet50 architecture demonstrated exceptional diagnostic performance (Fig. 4d and e), achieving an area under the ROC curve (AUC) of 0.994 on independent test set of 70 images (39 benign and 31 malignant). (Fig. 4f). It produced only one false positive and no false negatives, yielding an accuracy of 98.5 %, sensitivity of 100 %, specificity of 97.4 %, negative predictive value (NPV) of 100 %, positive predictive value (PPV) of 97.5 % and F1-score of 0.987. The raw ROC curve data and the confusion matrix are provided in the Supplementary Tables S1 and S2. Although sensitivity was 100 %, the false-positive case highlights the need to improve specificity using larger datasets and integrated multimodal information. The SRS imaging platform coupled with optimized deep learning establishes a robust framework for automated cervical cancer screening, combining subcellular chemical specificity with diagnostic-grade predictive accuracy.

3.5. *Multiplex cell segmentation for diagnostic decision support*

To complement AI-assisted malignancy detection with pathologist-interpretable visual guidance, we implemented a semantic segmentation framework (DeepLabV3+) for spatially resolving individual cancer cells within complex cytological mixtures. This architecture generates pixel-wise classifications of five cell types in SRS images, enabling precise identification of a few HSIL and SCC cells amidst a large number of mixed cells.

Pathologists created a gold-standard segmentation dataset through meticulous pixel-level annotation of 500 SRS images (Supplementary Fig. S3), partitioned into training (80 %) and test (20 %) sets. To address inherent diagnostic challenges in rare cancer cell identification, we strategically enriched the dataset to contain 62 % malignant images (Supplementary Fig. S4a) while maintaining biological relevance through controlled representation of cellular combinations (Supplementary Fig. S4b). The final distribution comprised 53.4 % SCC-containing and 43.2 % HSIL-containing images (Supplementary

Fig. S4c), ensuring robust exposure to key diagnostic targets.

The trained network is capable of distinguishing all five cell types in the same image field of view with high accuracy and high spatial resolution (Fig. 5a). The robust performance of the model in cell typing is shown under diverse combinations of cell mixtures (Fig. 5b). To quantitatively evaluate the segmentation capability of the network, four metrics are extracted and summarized in Table 1. Intersection over union (IoU): 0.76 ± 0.09 (mean ± SD), indicating strong spatial overlap with ground truth; Recall: 0.86 ± 0.07, demonstrating effective detection of pathological cells; Precision: 0.85 ± 0.08, confirming minimal false positive identifications; Dice coefficient: 0.84 ± 0.06, reflecting comprehensive segmentation accuracy [53].

Performance variation across cell types revealed fundamental biological correlations: Normal cells showed optimal segmentation (IoU = 0.88) due to distinct morphological signatures, while HSIL (IoU = 0.67) and SCC (IoU = 0.69) presented greater challenges from overlapping biochemical profiles (Fig. 5c). Such cell-type-dependence was found to be correlated with the cytologic features of each cell type as shown in the comparison between their R values (averaged with respect to the rest four types) and the model metrics (Fig. 5c). In particular, three key determinants of segmentation fidelity could be identified: cell size, lipid content and protein/lipid ratio. The biochemical-morphological coupling confirms the network leverages biologically meaningful features for decision-making. By integrating segmentation maps with diagnostic classifications, we establish a VAD-SRC platform that enhances clinical utility.

Traditional cytology relies on visual assessment of stained cell morphology, which is time-consuming with modest sensitivity (50–70 %) [54–58]. In contrast, spontaneous Raman spectroscopy suffers from weak signals and long acquisition times, whereas SRS microscopy provides rapid, label-free imaging at subcellular resolution, making it more suitable for high-throughput cytology. Our work demonstrates the advantage of combining quantitative chemical imaging and deep-learning algorithms in the rapid diagnostic classification of cervical cells in early cancer screening. This integration of SRS and AI offers both chemical specificity and diagnostic-grade performance, advancing beyond conventional methods of cytologic screening.

Although cervical exfoliated cells could be classified into numerous fine categories [59,60], in this work we simplified them into five grades with clinical significance [52,61]. Furthermore, according to the ACS

Table 1
Performance of the segmentation model. Intersection over union (IoU), recall, precision and dice coefficient were used as metrics to evaluate the performance of the segmentation model for different cell types.

Category	IoU	Recall	Precision	Dice
SCC	0.69	0.81	0.81	0.80
HSIL	0.67	0.82	0.77	0.78
LSIL	0.82	0.90	0,89	0.89
Leucocytes	0.73	0.83	0,85	0.83
Normal	0.88	0.92	0.93	0.92
Average	0.76	0.86	0.85	0.84

management guidelines, LSIL is typically managed conservatively as benign, whereas HSIL and SCC require definitive treatment. Hence, our binary classification strategy (benign vs. malignant) reflects clinical practice. Nevertheless, we acknowledge that increasing the classification categories are important in real-world diagnosis, and future extensions to multiclass models could enhance clinical applicability. Besides lipid and protein, other biochemical components such as glycogen may also be explored [62,63], but the trade-off between added information and imaging efficiency must be considered.

AI-assisted diagnostic techniques have significantly advanced and are widely applied in medicine [64–66]. In this study, image-based supervised learning outperformed feature-based unsupervised learning. A major challenge remains the need for extensive manual annotation, particularly with larger datasets. Weakly supervised learning emerges as a promising solution [31,67], may potentially improve diagnostic accuracy and reduce annotation workload. Despite current limitations of dataset size and inter-pathologist variability, segmentation performance has already met review standards for diagnostic support. To further assess scalability, we compared computational resource requirements between ResNet50 and DeepLabV3+, as summarized in Supplementary Table S3. These results indicate that while DeepLabV3+ offers finer spatial localization, the lighter ResNet50 is more resource-efficient.

In terms of diagnostic reliability, although our model achieved 100 % sensitivity on the independent test set, one benign case was misclassified as malignant, highlighting the possibility of false positives in clinical practice. To mitigate the risks, AI predictions should be integrated into multi-stage workflows verified by pathologists, and future work should incorporate larger and more diverse datasets to improve

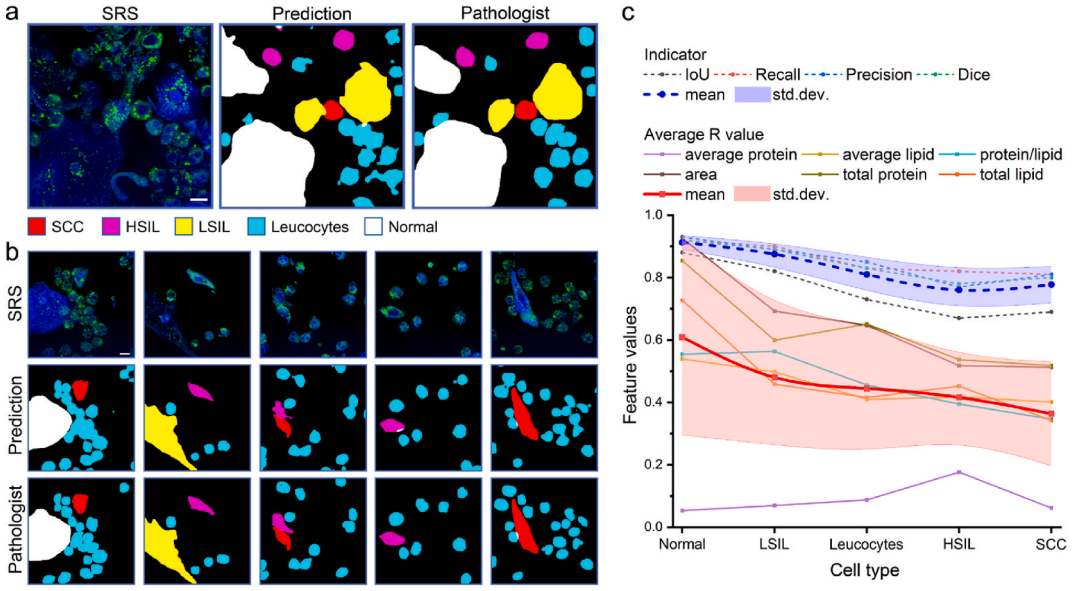

Fig. 5. Visual identification of cells using segmentation model. a, Comparison of the segmentation results using the deep-learning model with that of the pathologists on a mixture of five types of cervical cells. **b,** Demonstration of the effective identification of various cell types under diverse distributions using the model. Scale bars: 10 μ m. **c,** Correlation between the average R values of different cell types and the segmentation performance of the model.

specificity. Moreover, our current study involved 41 patients from a single institution, which may limit the generalizability of the findings and introduce potential institutional bias. Future multi-center cohort with larger data size are essential to strengthen the robustness of the method [68,69].

Beyond the innovative performance for cervical cytology, the applicability of VAD-SRC could also be extended to other similar cytological examinations, such as urinary, oral, and pleural fluid cytology. For clinical translation, further technical integration and cost reduction are necessary. Compact fiber-laser systems may replace bulky solid-state lasers [70,71], U-Net–based femto-SRS methods could simplify configuration [72], and virtual staining could transform SRS images into standard histopathologic formats [34,35,73]. Together with multicenter validation, these improvements could support routine adoption of VAD-SRC.

4. Conclusions

In summary, our study demonstrates the effectiveness of AI-assisted SRS microscopy for efficient cervical cytology analysis. The quantitative biochemical analysis identified distinct cytological features in various cell types that are strongly associated with malignancy. Our VAD-SRC system offers two key functions: rapid screening of cells to determine if they are benign or malignant with high accuracy, and the ability to automatically visualize individual cancer exfoliated cells, aiding pathologists in precise diagnosis. VAD-SRC holds promise to bridge the gap between AI-driven diagnostics and conventional cytopathology, ultimately enhancing diagnostic accuracy and efficiency in cervical cancer screening.

CRediT authorship contribution statement

Yingjie He: Writing – review & editing, Writing – original draft, Validation, Software, Methodology, Investigation, Formal analysis, Data curation. **Mingming Zhao:** Writing – original draft, Formal analysis, Data curation. **Hao Zhang:** Validation, Supervision, Resources. **Minbiao Ji:** Writing – review & editing, Writing – original draft, Resources, Project administration, Methodology, Investigation, Funding acquisition, Formal analysis, Conceptualization. **Chao Wang:** Writing – review & editing, Validation, Supervision, Resources, Methodology, Investigation, Funding acquisition.

Declaration of competing interest

The authors declare that they have no known competing financial interests or personal relationships that could have appeared to influence the work reported in this paper.

Acknowledgements

This research was funded by the National Key R&D Program of China (2021YFF0502900); National Natural Science Foundation of China (62425501, 81772777, 82273233); Technical Standardization Management and Promotion Project of SHDC (SHDC22025206); Research Project of the Shanghai Municipal Health Commission (202540070); "Medical Innovation Research" 2025 Shanghai Municipal Science and Technology Commission (25Y22800300); and Shanghai Key Laboratory of Female Reproductive Endocrine Related Diseases.

Appendix A. Supplementary data

Supplementary data to this article can be found online at https://doi.org/10.1016/j.talanta.2025.128982.

Y.H. and M.Z. contributed equally to this work. M.J. and C.W. conceived and designed the study. Y.H. performed SRS microscopy experiments and constructed deep learning algorithms and performed trainings. Y.H. and M.Z. performed SRS data collection and analysis. C. W. and M.Z. prepared the cell samples and helped medical data interpretation. H.Z. performed pathology work. M.J., C.W., Y.H., and M.Z. wrote the manuscript and all authors reviewed and approved it.

Data availability

Data will be made available on request.

References

[1] P.A. Cohen, A. Jhingran, A. Oaknin, L. Denny, Cervical cancer, Lancet 393 (10167) (2019) 169–182, https://doi.org/10.1016/S0140-6736(18)32470-X.
[2] R.L. Siegel, K.D. Miller, N.S. Wagle, A. Jemal, Cancer statistics, 2023, CA Cancer J. Clin. 73 (1) (2023) 17–48, https://doi.org/10.3322/caac.21763.
[3] Y. Zhang, Y. Wang, L. Liu, Y. Fan, Z. Liu, Y. Wang, S. Nie, Awareness and knowledge about human papillomavirus vaccination and its acceptance in China: a meta-analysis of 58 observational studies, BMC Public Health 16 (2016) 216, https://doi.org/10.1186/s12889-016-2873-8.
[4] X.F. Pan, R. Li, A. Pan, H. Larson, Human papillomavirus vaccine approval in China: a major step forward but challenges ahead, Lancet Infect. Dis. 16 (12) (2016) 1322–1323, https://doi.org/10.1016/S1473-3099(16)30450-9.
[5] J.F. Laprise, H.W. Chesson, L.E. Markowitz, M. Drolet, D. Martin, E. Benard, M. Brisson, Effectiveness and cost-effectiveness of human papillomavirus vaccination through age 45 years in the United States, Ann. Intern. Med. 172 (1) (2020) 22–29, https://doi.org/10.7326/M19-1182.
[6] F. Zhao, Y. Qiao, Cervical cancer prevention in China: a key to cancer control, Lancet 393 (10175) (2019) 969–970, https://doi.org/10.1016/S0140-6736(18)32849-6.
[7] R.B. Perkins, N. Wentzensen, R.S. Guido, M. Schiffman, Cervical cancer screening: a review, JAMA 330 (6) (2023) 547–558, https://doi.org/10.1001/jama.2023.13174.
[8] A.R. Bhatt, A. Ganatra, K. Kotecha, Cervical cancer detection in pap smear whole slide images using convNet with transfer learning and progressive resizing, PeerJ Comput. Sci. 7 (2021) e348, https://doi.org/10.7717/peerj-cs.348.
[9] R.P. Bosgraaf, A.G. Siebers, J.A. De Hullu, L.F. Massuger, J. Bulten, R.L. Bekkers, W.J. Melchers, The current position and the future perspectives of cervical cancer screening, Expert Rev. Anticancer Ther. 14 (1) (2014) 75–92, https://doi.org/10.1586/14737140.2014.856273.
[10] C. Chen, Z. Yang, Z. Li, L. Li, Accuracy of several cervical screening strategies for early detection of cervical cancer: a meta-analysis, Int. J. Gynecol. Cancer 22 (6) (2012) 908–921, https://doi.org/10.1097/IGC.0b013e318256e5e4.
[11] E.T.H. Fontham, A.M.D. Wolf, T.R. Church, R. Etzioni, C.R. Flowers, A. Herzig, C. E. Guerra, K.C. Oeffinger, Y.T. Shih, L.C. Walter, J.J. Kim, K.S. Andrews, C. E. DeSantis, S.A. Fedewa, D. Manassaram-Baptiste, D. Saslow, R.C. Wender, R. A. Smith, Cervical cancer screening for individuals at average risk: 2020 guideline update from the American cancer society, CA Cancer J. Clin. 70 (5) (2020) 321–346, https://doi.org/10.3322/caac.21628.
[12] L. Yan, X. Xiao, L. He, L. Shi, X. Yang, J. Zhang, Y. Zhang, C. Fu, Efficacy of optical coherence tomography in the triage of women with minor abnormal cervical cytology before colposcopy, PLoS One 18 (3) (2023) e0282833, https://doi.org/10.1371/journal.pone.0282833.
[13] T. Matsui, R. Tamoto, A. Iwasa, M. Mimura, S. Taniguchi, T. Hasegawa, T. Sudo, H. Mizuno, J. Kikuta, I. Onoyama, K. Okugawa, M. Shiomi, S. Matsuzaki, E. Morii, T. Kimura, K. Kato, Y. Kiyota, M. Ishii, Nonlinear optics with near-infrared excitation enable real-time quantitative diagnosis of human cervical cancers, Cancer Res. 80 (17) (2020) 3745–3754, https://doi.org/10.1158/0008-5472.CAN-20-0348.
[14] S. Rubina, M. Amita, R. Bharat, C.M. Krishna, Raman spectroscopic study on classification of cervical cell specimens, Vib. Spectrosc. 68 (2013) 115–121.
[15] I.R. Ramos, A.D. Meade, O. Ibrahim, H.J. Byrne, M. McMenamin, M. McKenna, A. Malkin, F.M. Lyng, Raman spectroscopy for cytopathology of exfoliated cervical cells, Faraday Discuss 187 (2016) 187–198, https://doi.org/10.1039/c5fd00197h.
[16] S. Duraipandian, D. Traynor, P. Kearney, C. Martin, J.J. O'Leary, F.M. Lyng, Raman spectroscopic detection of high-grade cervical cytology: using morphologically normal appearing cells, Sci. Rep. 8 (1) (2018) 15048, https://doi.org/10.1038/s41598-018-33417-8.
[17] K. Aljakouch, Z. Hilal, I. Daho, M. Schuler, S.D. Krauss, H.K. Yosef, J. Dierks, A. Mosig, K. Gerwert, S.F. El-Mashtoly, Fast and noninvasive fiagnosis of cervical cancer by coherent anti-stokes raman scattering, Anal. Chem. 91 (21) (2019) 13900–13906, https://doi.org/10.1021/acs.analchem.9b03395.
[18] D. Hanahan, Hallmarks of cancer: new dimensions, Cancer Discov. 12 (1) (2022) 31–46, https://doi.org/10.1158/2159-8290.CD-21-1059.
[19] B. Faubert, A. Solmonson, R.J. DeBerardinis, Metabolic reprogramming and cancer progression, Science 368 (6487) (2020), https://doi.org/10.1126/science.aaw5473.
[20] M.F. Mitchell, S.B. Cantor, N. Ramanujam, G. Tortolero-Luna, R. Richards-Kortum, Fluorescence spectroscopy for diagnosis of squamous intraepithelial lesions of the cervix, Obstet. Gynecol. 93 (3) (1999) 462–470, https://doi.org/10.1016/s0029-7844(98)00385-8.
[21] M. Ji, J. Zhong, R. Xue, W. Su, Y. Kong, Y. Fei, J. Ma, Y. Wang, L. Mi, Early detection of cervical cancer by fluorescence lifetime imaging microscopy combined

with unsupervised machine learning, Int. J. Mol. Sci. 23 (19) (2022) 11476, https://doi.org/10.3390/ijms231911476.
[22] K. Pandey, A. Pradhan, A. Agarwal, A. Bhagoliwal, N. Agarwal, Fluorescence spectroscopy: a new approach in cervical cancer, J. Obstet. Gynaecol. India 62 (4) (2012) 432–436, https://doi.org/10.1007/s13224-012-0298-6.
[23] D. Chokchaichamnankit, K. Watcharatanyatip, P. Subhasitanont, C. Weeraphan, S. Keeratichamroen, N. Sritana, N. Kantathavorn, P. Diskul-Na-Ayudthaya, K. Saharat, J. Chantaraamporn, C. Verathamjamras, N. Phoolcharoen, K. Wiriyaukaradecha, N.M. Paricharttanakul, W. Udomchaiprasertkul, T. Sricharunrat, C. Auewarakul, J. Svasti, C. Srisomsap, Urinary biomarkers for the diagnosis of cervical cancer by quantitative label-free mass spectrometry analysis, Oncol. Lett. 17 (6) (2019) 5453–5468, https://doi.org/10.3892/ol.2019.10227.
[24] S. Liu, Z. Yuan, X. Qiao, Q. Liu, K. Song, B. Kong, X. Su, Light scattering pattern specific convolutional network static cytometry for label-free classification of cervical cells, Cytometry A 99 (6) (2021) 610–621, https://doi.org/10.1002/cyto.a.24349.
[25] V. Karunakaran, V.N. Saritha, M.M. Joseph, J.B. Nair, G. Saranya, K.G. Raghu, K. Sujathan, K.S. Kumar, K.K. Maiti, Diagnostic spectro-cytology revealing differential recognition of cervical cancer lesions by label-free surface enhanced raman fingerprints and chemometrics, Nanomedicine 29 (2020) 102276, https://doi.org/10.1016/j.nano.2020.102276.
[26] F.M. Lyng, D. Traynor, I.R. Ramos, F. Bonnier, H.J. Byrne, Raman spectroscopy for screening and diagnosis of cervical cancer, Anal. Bioanal. Chem. 407 (27) (2015) 8279–8289, https://doi.org/10.1007/s00216-015-8946-1.
[27] C.W. Freudiger, W. Min, B.G. Saar, S. Lu, G.R. Holtom, C. He, J.C. Tsai, J.X. Kang, X.S. Xie, Label-free biomedical imaging with high sensitivity by stimulated Raman scattering microscopy, Science 322 (5909) (2008) 1857–1861, https://doi.org/10.1126/science.1165758.
[28] L. Shi, M. Wei, Y. Miao, N. Qian, L. Shi, R.A. Singer, R.K.P. Benninger, W. Min, Highly-multiplexed volumetric mapping with Raman dye imaging and tissue clearing, Nat. Biotechnol. 40 (3) (2022) 364–373, https://doi.org/10.1038/s41587-021-01041-z.
[29] M. Ji, M. Arbel, L. Zhang, C.W. Freudiger, S.S. Hou, D. Lin, X. Yang, B.J. Bacskai, X. S. Xie, Label-free imaging of amyloid plaques in Alzheimer's disease with stimulated Raman scattering microscopy, Sci. Adv. 4 (11) (2018) eaat7715, https://doi.org/10.1126/sciadv.aat7715.
[30] Q. Cheng, Y. Miao, J. Wild, W. Min, Y. Yang, Emerging applications of stimulated Raman scattering microscopy in materials science, Matter 4 (5) (2021) 1460–1483, https://doi.org/10.1016/j.matt.2021.02.013.
[31] Y. Yang, Z. Liu, J. Huang, X. Sun, J. Ao, B. Zheng, W. Chen, Z. Shao, H. Hu, Y. Yang, M. Ji, Histological diagnosis of unprocessed breast core-needle biopsy via stimulated Raman scattering microscopy and multi-instance learning, Theranostics 13 (4) (2023) 1342–1354, https://doi.org/10.7150/thno.81784.
[32] L. Ma, K. Luo, Z. Liu, M. Ji, Stain-free histopathology with stimulated Raman scattering microscopy, Anal. Chem. 96 (20) (2024) 7907–7925, https://doi.org/10.1021/acs.analchem.4c02061.
[33] A. Kondepudi, M. Pekmezci, X. Hou, K. Scotford, C. Jiang, A. Rao, E.S. Harake, A. Chowdury, W. Al-Holou, L. Wang, A. Pandey, P.R. Lowenstein, M.G. Castro, L. I. Koerner, T. Roetzer-Pejrimovsky, G. Widhalm, S. Camelo-Piragua, M. Movahed-Ezazi, D.A. Orringer, H. Lee, C. Freudiger, M. Berger, S. Hervey-Jumper, T. Hollon, Foundation models for fast, label-free detection of glioma infiltration, Nature 637 (8045) (2025) 439–445, https://doi.org/10.1038/s41586-024-08169-3.
[34] T. Fang, Z. Wu, X. Chen, L. Tan, Z. Li, J. Ji, Y. Fan, Z. Li, S. Yue, Label-free virtual peritoneal lavage cytology via deep-learning-assisted single-color stimulated Raman scattering microscopy, Adv. Intell. Syst. 6 (5) (2024) 2300689, https://doi.org/10.1002/aisy.202300689.
[35] Z. Liu, L. Chen, H. Cheng, J. Ao, J. Xiong, X. Liu, Y. Chen, Y. Mao, M. Ji, Virtual formalin-fixed and paraffin-embedded staining of fresh brain tissue via stimulated Raman CycleGAN model, Sci. Adv. 10 (13) (2024) eadn3426, https://doi.org/10.1126/sciadv.adn3426.
[36] H. Lin, S. Seitz, Y. Tan, J.B. Lugagne, L. Wang, G. Ding, H. He, T.J. Rauwolf, M. J. Dunlop, J.H. Connor, J.A. Porco Jr., L. Tian, J.X. Cheng, Label-free nanoscopy of cell metabolism by ultrasensitive reweighted visible stimulated Raman scattering, Nat. Methods 22 (5) (2025) 1040–1050, https://doi.org/10.1038/s41592-024-02575-1.
[37] X. Chen, Z. Wu, Y. He, Z. Hao, Q. Wang, K. Zhou, W. Zhou, P. Wang, F. Shan, Z. Li, J. Ji, Y. Fan, Z. Li, S. Yue, Accurate and rapid detection of peritoneal metastasis from gastric cancer by AI-assisted stimulated raman molecular cytology, Adv. Sci. 10 (21) (2023) e2300961, https://doi.org/10.1002/advs.202300961.
[38] G. Sangalli, G. Serio, C. Zampatti, M. Bellotti, G. Lomuscio, Fine needle aspiration cytology of the thyroid: a comparison of 5469 cytological and final histological diagnoses, Cytopathology 17 (5) (2006) 245–250, https://doi.org/10.1111/j.1365-2303.2006.00335.x.
[39] J.G. Jonasson, H.H. Wang, D.H. Porter, G. Tyagi, B.S. Ducatman, Image-directed percutaneous biopsy. A comparison of cytologic and histologic findings, Cancer 70 (8) (1992) 2187–2191, https://doi.org/10.1002/1097-0142(19921015)70:8<2187::aid-cncr2820700829>3.0.co;2-3.
[40] M.K. Sidawy, D.M. Del Vecchio, S.M. Knoll, Fine-needle aspiration of thyroid nodules: correlation between cytology and histology and evaluation of discrepant cases, Cancer 81 (4) (1997) 253–259, https://doi.org/10.1002/(sici)1097-0142(19970825)81:4<253::aid-cncr7>3.0.co;2-q.
[41] L. Pantanowitz, M. Hornish, R.A. Goulart, The impact of digital imaging in the field of cytopathology, CytoJournal 6 (2009) 6, https://doi.org/10.4103/1742-6413.48606.
[42] S.W. Jahn, M. Plass, F. Moinfar, Digital pathology: advantages, limitations and emerging perspectives, J. Clin. Med. 9 (11) (2020) 3697, https://doi.org/10.3390/jcm9113697.
[43] Z. Huang, E. Yang, J. Shen, D. Gratzinger, F. Eyerer, B. Liang, J. Nirschl, D. Bingham, A.M. Dussaq, C. Kunder, R. Rojansky, A. Gilbert, A.L. Chang-Graham, B.E. Howitt, Y. Liu, E.E. Ryan, T.B. Tenney, X. Zhang, A. Folkins, E.J. Fox, K. S. Montine, T.J. Montine, J. Zou, A pathologist-AI collaboration framework for enhancing diagnostic accuracies and efficiencies, Nat. Biomed. Eng. 9 (4) (2025) 455–470, https://doi.org/10.1038/s41551-024-01223-5.
[44] M.K.K. Niazi, A.V. Parwani, M.N. Gurcan, Digital pathology and artificial intelligence, Lancet Oncol. 20 (5) (2019) e253–e261, https://doi.org/10.1016/S1470-2045(19)30154-8.
[45] F.K. Lu, S. Basu, V. Igras, M.P. Hoang, M. Ji, D. Fu, G.R. Holtom, V.A. Neel, C. W. Freudiger, D.E. Fisher, X.S. Xie, Label-free DNA imaging in vivo with stimulated Raman scattering microscopy, Proc. Natl. Acad. Sci. USA. 112 (37) (2015) 11624–11629, https://doi.org/10.1073/pnas.1515121112.
[46] M. Ji, S. Lewis, S. Camelo-Piragua, S.H. Ramkissoon, M. Snuderl, S. Venneti, A. Fisher-Hubbard, M. Garrard, D. Fu, A.C. Wang, J.A. Heth, C.O. Maher, N. Sanai, T.D. Johnson, C.W. Freudiger, O. Sagher, X.S. Xie, D.A. Orringer, Detection of human brain tumor infiltration with quantitative stimulated Raman scattering microscopy, Sci. Transl. Med. 7 (309) (2015) 309ra163, https://doi.org/10.1126/scitranslmed.aab0195.
[47] F.K. Lu, M. Ji, D. Fu, X. Ni, C.W. Freudiger, G. Holtom, X.S. Xie, Multicolor stimulated Raman scattering (SRS) microscopy, Mol. Phys. 110 (15–16) (2012) 1927–1932, https://doi.org/10.1080/00268976.2012.695028.
[48] D. Fu, F.K. Lu, X. Zhang, C. Freudiger, D.R. Pernik, G. Holtom, X.S. Xie, Quantitative chemical imaging with multiplex stimulated Raman scattering microscopy, J. Am. Chem. Soc. 134 (8) (2012) 3623–3626, https://doi.org/10.1021/ja210081h.
[49] C.W. Freudiger, R. Pfannl, D.A. Orringer, B.G. Saar, M. Ji, Q. Zeng, L. Ottoboni, Y. Wei, C. Waeber, J.R. Sims, P.L. De Jager, O. Sagher, M.A. Philbert, X. Xu, S. Kesari, X.S. Xie, G.S. Young, Multicolored stain-free histopathology with coherent Raman imaging, Lab. Invest. 92 (10) (2012) 1492–1502, https://doi.org/10.1038/labinvest.2012.109.
[50] A. Alrajjal, V. Pansare, M.S.R. Choudhury, M.Y.A. Khan, V.B. Shidham, Squamous intraepithelial lesions (SIL: LSIL, HSIL, ASCUS, ASC-H, LSIL-H) of uterine cervix and Bethesda system, CytoJournal 18 (2021) 16, https://doi.org/10.25259/Cytojournal_24_2021.
[51] M.J. Thrall, A practical approach to squamous abnormalities on cervical cytology: overview of interpretive criteria and guidance for altering thresholds in response to quality assurance findings, Acta Cytol. 67 (2) (2023) 129–142, https://doi.org/10.1159/000528531.
[52] J. Wang, Y. Yu, Y. Tan, H. Wan, N. Zheng, Z. He, L. Mao, W. Ren, K. Chen, Z. Lin, G. He, Y. Chen, R. Chen, H. Xu, K. Liu, Q. Yao, S. Fu, Y. Song, Q. Chen, L. Zuo, L. Wei, J. Wang, N. Ouyang, H. Yao, Artificial intelligence enables precision diagnosis of cervical cytology grades and cervical cancer, Nat. Commun. 15 (1) (2024) 4369, https://doi.org/10.1038/s41467-024-48705-3.
[53] Z. Wang, E. Wang, Y. Zhu, Image segmentation evaluation: a survey of methods, Artif. Intell. Rev. 53 (8) (2020) 5637–5674.
[54] H.C. Kitchener, R. Blanks, G. Dunn, L. Gunn, M. Desai, R. Albrow, J. Mather, D. N. Rana, H. Cubie, C. Moore, R. Legood, A. Gray, S. Moss, Automation-assisted versus manual reading of cervical cytology (MAVARIC): a randomised controlled trial, Lancet Oncol. 12 (1) (2011) 56–64, https://doi.org/10.1016/S1470-2045(10)70264-3.
[55] D.C. McCrory, D.B. Matchar, L. Bastian, S. Datta, V. Hasselblad, J. Hickey, E. Myers, K. Nanda, Evaluation of cervical cytology, Evid. Rep. Technol. Assess. (5) (1999) 1–6.
[56] M.T. Fahey, L. Irwig, P. Macaskill, Meta-analysis of Pap test accuracy, Am. J. Epidemiol. 141 (7) (1995) 680–689, https://doi.org/10.1093/oxfordjournals.aje.a117485.
[57] L.G. Koss, The Papanicolaou test for cervical cancer detection. A triumph and a tragedy, JAMA 261 (5) (1989) 737–743.
[58] K. Nanda, D.C. McCrory, E.R. Myers, L.A. Bastian, V. Hasselblad, J.D. Hickey, D. B. Matchar, Accuracy of the Papanicolaou test in screening for and follow-up of cervical cytologic abnormalities: a systematic review, Ann. Intern. Med. 132 (10) (2000) 810–819, https://doi.org/10.7326/0003-4819-132-10-200005160-00009.
[59] R. Nayar, D.C. Wilbur, The Pap test and Bethesda 2014, Cancer. Cytopathol. 123 (5) (2015) 271–281, https://doi.org/10.1002/cncy.21521.
[60] E. Hussain, L.B. Mahanta, C.R. Das, M. Choudhury, M. Chowdhury, A shape context fully convolutional neural network for segmentation and classification of cervical nuclei in Pap smear images, Artif. Intell. Med. 107 (2020) 101897, https://doi.org/10.1016/j.artmed.2020.101897.
[61] C.W. Wang, Y.A. Liou, Y.J. Lin, C.C. Chang, P.H. Chu, Y.C. Lee, C.H. Wang, T. K. Chao, Artificial intelligence-assisted fast screening cervical high grade squamous intraepithelial lesion and squamous cell carcinoma diagnosis and treatment planning, Sci. Rep. 11 (1) (2021) 16244, https://doi.org/10.1038/s41598-021-95545-y.
[62] W.B. Ayre, J.E. Ayre, Cytochemical study of glycogen in the diagnosis of cervical cancer, Am. J. Clin. Pathol. 20 (7) (1950) 644–650, https://doi.org/10.1093/ajcp/20.7.644.
[63] W.B. Ayre, The glycogen-estrogen relationship in the vaginal tract, J. Clin. Endocrinol. Metab. 11 (1) (1951) 103–110, https://doi.org/10.1210/jcem-11-1-103.
[64] O. Elemento, C. Leslie, J. Lundin, G. Tourassi, Artificial intelligence in cancer research, diagnosis and therapy, Nat. Rev. Cancer 21 (12) (2021) 747–752, https://doi.org/10.1038/s41568-021-00399-1.

[65] M.Y. Lu, B. Chen, D.F.K. Williamson, R.J. Chen, M. Zhao, A.K. Chow, K. Ikemura, A. Kim, D. Pouli, A. Patel, A. Soliman, C. Chen, T. Ding, J.J. Wang, G. Gerber, I. Liang, L.P. Le, A.V. Parwani, L.L. Weishaupt, F. Mahmood, A multimodal generative AI copilot for human pathology, Nature 634 (8033) (2024) 466–473, https://doi.org/10.1038/s41586-024-07618-3.

[66] M. Moor, O. Banerjee, Z.S.H. Abad, H.M. Krumholz, J. Leskovec, E.J. Topol, P. Rajpurkar, Foundation models for generalist medical artificial intelligence, Nature 616 (7956) (2023) 259–265, https://doi.org/10.1038/s41586-023-05881-4.

[67] G. Campanella, M.G. Hanna, L. Geneslaw, A. Miraflor, V. Werneck Krauss Silva, K. J. Busam, E. Brogi, V.E. Reuter, D.S. Klimstra, T.J. Fuchs, Clinical-grade computational pathology using weakly supervised deep learning on whole slide images, Nat. Med. 25 (8) (2019) 1301–1309, https://doi.org/10.1038/s41591-019-0508-1.

[68] J. Guo, B. Li, The application of medical artificial intelligence technology in rural areas of developing countries, Health. Equity 2 (1) (2018) 174–181, https://doi.org/10.1089/heq.2018.0037.

[69] P. Strom, K. Kartasalo, H. Olsson, L. Solorzano, B. Delahunt, D.M. Berney, D. G. Bostwick, A.J. Evans, D.J. Grignon, P.A. Humphrey, K.A. Iczkowski, J.G. Kench, G. Kristiansen, T.H. van der Kwast, K.R.M. Leite, J.K. McKenney, J. Oxley, C.C. Pan, H. Samaratunga, J.R. Srigley, H. Takahashi, T. Tsuzuki, M. Varma, M. Zhou, J. Lindberg, C. Lindskog, P. Ruusuvuori, C. Wahlby, H. Gronberg, M. Rantalainen, L. Egevad, M. Eklund, Artificial intelligence for diagnosis and grading of prostate cancer in biopsies: a population-based, diagnostic study, Lancet Oncol. 21 (2) (2020) 222–232, https://doi.org/10.1016/S1470-2045(19)30738-7.

[70] D.A. Orringer, B. Pandian, Y.S. Niknafs, T.C. Hollon, J. Boyle, S. Lewis, M. Garrard, S.L. Hervey-Jumper, H.J.L. Garton, C.O. Maher, J.A. Heth, O. Sagher, D. A. Wilkinson, M. Snuderl, S. Venneti, S.H. Ramkissoon, K.A. McFadden, A. Fisher-Hubbard, A.P. Lieberman, T.D. Johnson, X.S. Xie, J.K. Trautman, C.W. Freudiger, S. Camelo-Piragua, Rapid intraoperative histology of unprocessed surgical specimens via fibre-laser-based stimulated Raman scattering microscopy, Nat. Biomed. Eng. 1 (2) (2017) 27, https://doi.org/10.1038/s41551-016-0027.

[71] T. Hollon, C. Jiang, A. Chowdury, M. Nasir-Moin, A. Kondepudi, A. Aabedi, A. Adapa, W. Al-Holou, J. Heth, O. Sagher, P. Lowenstein, M. Castro, L.I. Wadiura, G. Widhalm, V. Neuschmelting, D. Reinecke, N. von Spreckelsen, M.S. Berger, S. L. Hervey-Jumper, J.G. Golfinos, M. Snuderl, S. Camelo-Piragua, C. Freudiger, H. Lee, D.A. Orringer, Artificial-intelligence-based molecular classification of diffuse gliomas using rapid, label-free optical imaging, Nat. Med. 29 (4) (2023) 828–832, https://doi.org/10.1038/s41591-023-02252-4.

[72] Z. Liu, W. Su, J. Ao, M. Wang, Q. Jiang, J. He, H. Gao, S. Lei, J. Nie, X. Yan, X. Guo, P. Zhou, H. Hu, M. Ji, Instant diagnosis of gastroscopic biopsy via deep-learned single-shot femtosecond stimulated Raman histology, Nat. Commun. 13 (1) (2022) 4050, https://doi.org/10.1038/s41467-022-31339-8.

[73] B. Shen, Z. Li, Y. Pan, Y. Guo, Z. Yin, R. Hu, J. Qu, L. Liu, Noninvasive nonlinear optical vomputational histology, Adv. Sci. 11 (9) (2024) e2308630, https://doi.org/10.1002/advs.202308630.